Laser-Assisted Milling of Silicon Nitride Ceramics and Inconel 718

Yinggang Tian

Benxin Wu

Mark Anderson

Yung C. Shin

Center for Laser-Based Manufacturing,
Purdue University,
West Lafayette, IN 47907

Laser-assisted machining (LAM) has shown its potential to significantly reduce fabrication costs and improve product quality for advanced materials. While extensive studies have been conducted on laser-assisted turning of various ceramics and high temperature alloys, few attempts have been made to extend LAM to milling operations. In this paper, a transient, three-dimensional thermal model developed for laser-assisted milling (LAML) is presented and its accuracy is verified by surface temperature measurements with an infrared camera. LAML experiments designed by the model are successfully conducted on silicon nitride ceramics using TiAlN coated carbide end mills and Inconel 718 using SiC reinforced alumina cutting tools. The promising experimental results, including good surface roughness and acceptable tool wear, show the validation of applying the thermal model to design LAML processes and the feasibility of employing LAML for difficult-to-machine materials such as advanced ceramics and superalloys.
[DOI: 10.1115/1.2927447]

1 Introduction

Laser-assisted machining (LAM) has been proposed as a promising technique to fabricate difficult-to-machine materials such as advanced ceramics [1–6] and high temperature alloys [7–11]. During LAM, the workpiece is locally heated by a controllable laser beam and then shaped with a conventional cutting tool. By locally heating and softening workpiece, LAM can significantly improve the machinability of workpiece material and hence produce good machining results. With the growing interest in LAM, extensive experimental investigations have been conducted on laser-assisted turning (LAT) of various ceramics, such as silicon nitride [6,12], mullite [13], and magnesia-partially stabilized zirconia (PSZ) [14]. Those experimental studies have shown the feasibility of LAT and its advantages over conventional machining methods in terms of surface finish, tool wear, specific cutting energy, and subsurface integrity for various ceramic materials. To facilitate the design and analysis of LAT processes, transient, three-dimensional thermal models have been developed for LAT of opaque [15,16], semitransparent [17], and complex workpieces [18].

Recently, a series of successful LAM results with various difficult-to-machine metals have also been reported. Based on a systematic modeling tools and use of cost-effective surface coating techniques, LAM could be applied to various metals without requiring very high laser power, which made LAM unattractive in the earlier studies. Skvarenina and Shin [19] applied LAM to improve the machinability of compacted graphite iron, while maintaining the microstructure of the machined surface unaffected during LAM. Anderson et al. [10] demonstrated the significant improvement in the machinability of Inconel 718 with economic benefits. Anderson and Shin [11] also showed the application of LAM to P550, which is another difficult-to-machine stainless steel due to its high nitrogen content. Again, by carefully controlling the temperature field predicted based on the numerical model, they were able to achieve virtually unchanged subsurface in microstructure and hardness, while significantly improving tool life and surface finish.

While extensive studies have been conducted on LAT, few attempts have been made on laser-assisted milling (LAML). The feasibility of LAML was shown by König and Zaboklicki [1] on a difficult-to-machine material, stellite 6. Recently, Jeon and Pfefferkorn [20] applied LAML to micromilling of 6061-T6 aluminum and 1018 steel. The authors experimentally found that laser could significantly improve the productivity of micromilling for the two investigated materials. Shen et al. [21] developed a finite element model to simulate the temperature and stress fields during LAML of silicon nitride. However, no experiment has been conducted. The present paper expands the capability of LAM to milling operations by developing a transient, three-dimensional thermal model and showing the applicability of LAML to silicon nitride and Inconel 718 through experiments via systematic design using the developed thermal model.

Manuscript received February 8, 2007; final manuscript received March 6, 2008; published online June 3, 2008. Review conducted by William J. Endres. Paper presented at the 2006 International Conference on Manufacturing Science and Engineering (MSEC2006), Ypsilanti, MI, October 8–11, 2006.

2 Thermal Modeling of Laser-Assisted Milling

The heat transfer problem associated with LAML of a prismatic workpiece is illustrated in Fig. 1, where complex transient boundaries and continuous material removal occur. The present thermal model is governed by the energy diffusion equation with temperature dependent material thermophysical properties:

$$\frac{\partial h(T)}{\partial t} = \frac{\partial}{\partial x}\left(k(T)\frac{\partial T}{\partial x}\right) + \frac{\partial}{\partial y}\left(k(T)\frac{\partial T}{\partial y}\right) + \frac{\partial}{\partial z}\left(k(T)\frac{\partial T}{\partial z}\right) \quad (1)$$

where the term on the left-hand side represents energy storage, and the three terms on the right-hand side stand for energy diffusion in the x, y, and z directions, respectively.

The thermal model used the temperature dependent thermophysical properties measured by Thermophysical Properties Research Laboratory, Inc. [22] for sintered silicon nitride, while the experimental study was conducted on sintered reaction-bonded silicon nitride. The present study assumes that the two types of silicon nitride have similar thermophysical properties, since they have almost identical chemical composition and microstructure.

The initial condition in the thermal model is given by the initial workpiece temperature before LAML, T_{ini}.

$$T(x,y,z,t=0) = T_{\text{ini}} \quad (2)$$

For the surface under the laser irradiation, Eq. (3) is used to account for the heat flux into the workpiece through laser irradiation, convection, and radiation. The spatial distribution of the laser energy on the workpiece, $q''_{\ell}(x,y)$, is determined by the actual beam profile. The heat flux through convection, q''_{conv}, is determined by free convection. The radiation exchange between the workpiece and the surrounding is represented by the heat flux, q''_{rad}, which is calculated using the instant workpiece surface tem-

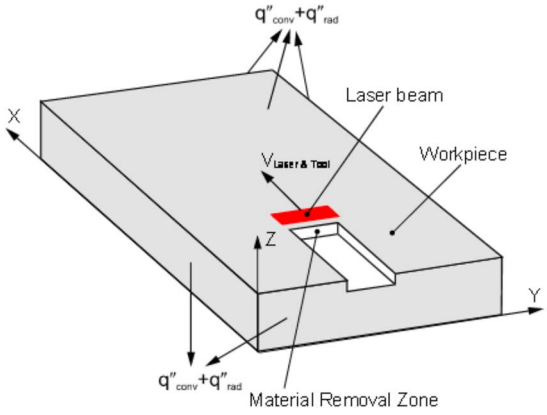

Fig. 1 Sketch of the modeled LAML

perature, ambient temperature, and the emissivity of workpiece material.

$$k \left.\frac{\partial T}{\partial z}\right|_{z=z_T} = \alpha_\ell q''_\ell(x,y) - q''_{\text{conv}} - q''_{\text{rad}} \tag{3}$$

For the portion of the top workpiece surface outside the laser irradiation, Eq. (3) reduces to

$$k \left.\frac{\partial T}{\partial z}\right|_{z=z_T} = - q''_{\text{conv}} - q''_{\text{rad}} \tag{4}$$

Similar to Eq. (3), boundary conditions with free convection and radiation are applied at other surfaces of the workpiece exposed to the environment. The free convection coefficient was assumed to be a temperature independent value of 10 $\text{W}/(\text{m}^2\,\text{K})$.

$$k \left.\frac{\partial T}{\partial x}\right|_{\substack{x=0\\x=x_L}} = - q''_{\text{conv}} - q''_{\text{rad}} \tag{5}$$

$$k \left.\frac{\partial T}{\partial y}\right|_{\substack{y=0\\y=y_W}} = - q''_{\text{conv}} - q''_{\text{rad}} \tag{6}$$

At the bottom surface of the workpiece, adiabatic boundary condition is assumed, when the workpiece sits on insulation materials.

$$\left.\frac{\partial T}{\partial z}\right|_{z=0} = 0 \tag{7}$$

At the material removal zone, thermal energy is generated due to material plastic deformation and tool-workpiece friction. Because the model does not include the tool, the interaction between the cutting tool and workpiece is considered by a heat flux into the workpiece as described in Eq. (8) for the heat transfer problem.

$$k \left.\frac{\partial T}{\partial x}\right|_{x=x_m} = q''_m \tag{8}$$

It has been shown that the heat generation associated with machining, q''_m, may be empirically obtained from the measured cutting forces for a given LAM process [18]. In general, the heat generation from machining is much less than the energy input from the laser.

During LAML, the workpiece geometry changes with the machining process. The instant geometry of the machined workpiece is calculated from the machining parameters. For instance, the width and depth of the machined slot are determined by the diameter of the end mill and the depth of cut.

2.1 Numerical Procedure. The explicit control volume method is applied in the current model. Each mesh cell (control volume) is in rectangular shape and has six cell surfaces. The cell surface is located in the middle of two adjacent cell centers. The grid spacing (the distance between cell centers) is nonuniform in the z direction and is uniform in the x and y directions. In laser heating, the temperature gradient in the region close to the $z=0$ surface is very high, and therefore small grid spacing is required to get accurate results. However, for the regions far away from the $z=0$ surface, the temperature gradient drops very quickly, and relatively large grid spacing is sufficient. Therefore, to save computational time, a nonuniform grid is applied such that the grid spacing in the z direction becomes larger as the z coordinate increases.

Next, the discrete equation for the governing equation is derived mathematically [23]. The integration of Eq. (1) over each control volume $V_{i,j,m}$ and time Δt yields

$$\int_t^{t+\Delta t}\int_{V_{i,j,m}} \frac{\partial H}{\partial t} dv dt = \int_t^{t+\Delta t}\int_{V_{i,j,m}} \left[\frac{\partial}{\partial x}\left(k(T)\frac{\partial T}{\partial x}\right) + \frac{\partial}{\partial y}\left(k(T)\frac{\partial T}{\partial y}\right) + \frac{\partial}{\partial z}\left(k(T)\frac{\partial T}{\partial z}\right)\right] dv dt \tag{9}$$

$$\int_t^{t+\Delta t}\int_{V_{i,j,m}} \frac{\partial H}{\partial t} dv dt = \int_t^{t+\Delta t}\int_{V_{i,j,m}} \nabla \cdot (-\mathbf{q}) dv dt \tag{10}$$

where $\mathbf{q}=-k\nabla T$ is the heat flux vector. By applying divergent theorem, the following can be obtained from Eq. (10):

$$\int_t^{t+\Delta t}\int_{V_{i,j,m}} \frac{\partial H}{\partial t} dv dt = \int_t^{t+\Delta t}\int_s (-\mathbf{q})\cdot \mathbf{ds} dt \tag{11}$$

where **ds** is the differential surface vector of the control volume pointing outward.

The integration with time on the right side of the equation is calculated approximately by assuming that $(-\mathbf{q}\cdot\mathbf{ds})$ remains the same value at t during the time interval $[t, t+\Delta t]$:

$$\int_{V_{i,j,m}} [H(t+\Delta t) - H(t)] dv = \Delta t \left\{\int_s (-\mathbf{q})\cdot \mathbf{ds}\right\}^t \tag{12}$$

The integration with volume on the left side of Eq. (12) is calculated approximately by assuming that H is uniform in each control volume, and the integration on the right side is calculated approximately by assuming that **q** is uniform on each of the six surfaces of the control volume and is equal to the value at the surface center.

Based on the above approximation, the following can be obtained:

$$[H(t+\Delta t) - H(t)] V_{i,j,m} = \Delta t \left(\sum_{l=1}^{6} q_l(t) s_l\right) \tag{13}$$

or

$$H(t+\Delta t) = H(t) + \frac{\Delta t}{V_{i,j,m}}\left(\sum_{l=1}^{6} q_l(t) s_l\right) \tag{14}$$

where $q_l(t)$ is the heat flux into the control volume at each surface at time t, and s_l is the area of each surface.

For all mesh cells, Eq. (14) can be rewritten as

$$H^{n+1}{}_{i,j,m} = H^n{}_{i,j,m} + \frac{\Delta t}{V_{i,j,m}}[(q_1+q_2)Sx_{j,m} + (q_3+q_4)Sy_{m,i} + (q_5+q_6)Sz_{i,j}] \tag{15}$$

The subscripts i, j, and m are indices of x, y, and z coordinates, respectively. $H^{n+1}{}_{i,j,m}$ is the enthalpy (per unit volume) at time step $n+1$ for the grip cell whose center is located at ($x[i]$, $y[j]$, $z[m]$), $H^n{}_{i,j,m}$ is the enthalpy at time step n, Δt is the time step

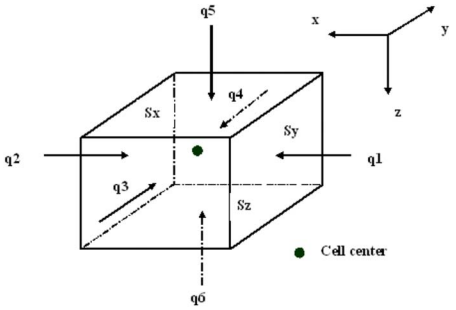

Fig. 2 The heat flux into a mesh cell

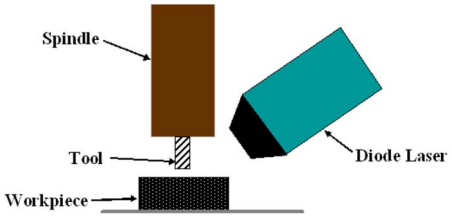

Fig. 3 Schematic of the LAML setup

length, and $V_{i,j,m}$ is the volume of the grid cell. q_1 and q_2 are the heat fluxes (per unit area and per unit time) into the grid cell along the x direction, q_3 and q_4 are along the y direction, and q_5 and q_6 are along the z direction. $Sx_{j,m}$ is the area of the cell face with the normal vector in the x direction, $Sy_{m,i}$ in the y direction, and $Sz_{i,j}$ in the z direction. See Fig. 2 for an illustration of q and S.

The conductivity k used in the expressions for q_1-q_6 is the value on the cell surface, and can be calculated based on the conductivities of the adjacent cell centers as follows [23]:

$$k_{\text{ave1}} = \frac{2k_{i-1,j,m}k_{i,j,m}}{k_{i-1,j,m}+k_{i,j,m}}, \quad k_{\text{ave2}} = \frac{2k_{i+1,j,m}k_{i,j,m}}{k_{i+1,j,m}+k_{i,j,m}}$$

$$k_{\text{ave3}} = \frac{2k_{i,j-1,m}k_{i,j,m}}{k_{i,j-1,m}+k_{i,j,m}}, \quad k_{\text{ave4}} = \frac{2k_{i,j+1,m}k_{i,j,m}}{k_{i,j+1,m}+k_{i,j,m}}$$

$$k_{\text{ave5}} = \frac{2k_{i,j,m-1}k_{i,j,m}}{k_{i,j,m-1}+k_{i,j,m}}, \quad k_{\text{ave6}} = \frac{2k_{i,j,m+1}k_{i,j,m}}{k_{i,j,m+1}+k_{i,j,m}} \tag{16}$$

where $k_{i,j,m}$ is the conductivity of the workpiece material at the temperature $T^n_{i,j,m}$.

Once the enthalpy for time step $n+1$ is calculated, the temperature for time step $n+1$ is obtained based on the enthalpy-temperature relation for a given material. The discrete equation for each cell is not coupled, and therefore no simultaneous equations need to be solved. From Eq. (15), the temperature for the next time step can be obtained cell by cell separately.

For the numerical solution, a fully implicit finite-volume method is used to discretize the governing equation, and the modeled domain is divided into a set of predefined, structured control volumes. A typical $100\times80\times9$ mm^3 workpiece is modeled by $160\times80\times42$ mesh in the x, y, and z directions, respectively. It is shown in grid sensitivity study that doubling the control volume number in each direction, respectively, resulted in a negligible change in the simulated temperature field. The numerical model is realized using the C language and solved iteratively with one sweep per iteration through the domain in the positive and negative directions of each coordinate. After each iteration, the new temperature field is used to update the temperature dependent variables, such as conductivity and specific heat of the workpiece material. To simulate the material removal during LAML, the present model continuously examines the geometry of the workpiece, identifies the control volumes corresponding to the workpiece material removed by the cutting tool, and then excludes those control volumes from the thermal model by setting the conductivity of those control volumes to zero.

3 Experimental Facilities and Test Matrix

3.1 Experimental Facilities. The LAML experiments were conducted on a five-axis gantry milling machine equipped with a 40,000 rpm precise high speed spindle. The laser source is a Nuvonyx 4 kW direct diode laser, which can generate a rectangular laser beam with the spot size of 12×8 mm^2 at the focus plane. The laser head was mounted on a Panasonic six-axis robot to provide necessary flexibility of adjusting the laser beam position, as shown in Fig. 3. Custom integration was made between the gantry milling machine and the diode laser to ensure the synchronization of the two subsystems during LAML.

The $100\times80\times9$ mm^3 rectangular workpieces used in the LAML experiments were made of sintered reaction-bonded silicon nitride. LAML of silicon nitride was carried out using TiAlN coated solid carbide end mills. The end mill has a diameter of 6 mm with two flutes. Experiments were also performed with Inconel 718 to determine feasibility and possible operating conditions for LAML. A single WG-300 insert (SPGN-21.52 T1A) with a 0.8 mm nose radius, a positive rake angle of 5 deg, a radial angle of 0 deg, and a side cutting angle of 15 deg was used on a 12.7 mm diameter end mill for slotting. The preheating cycle was maintained at 3 s for all machining tests.

An infrared camera (FLIR Systems, Model SC3000) was used to measure the surface temperature fields for the thermal model validation. For the measuring range of 350–1500°C, the accuracy of the infrared camera is specified to be $\pm2\%$ of the measured values in Celsius. Within the operating wavelength of the infrared camera, i.e., 8–9 μm, silicon nitride is considered opaque and the total emissivity is determined to be 0.95 from room temperature to 1450°C [24,25]. The wavelength of the diode laser, 808 nm, is far away from the wavelength detected by the infrared camera (8–9 μm), and hence the reflected laser irradiation has no influence on the measured temperature field. For Inconel 718, the absorptivity of the workpiece was determined using the method described by Anderson et al. [10]. Table 1 lists those properties used in the present study for silicon nitride and Inconel 718.

3.2 Test Matrix for Thermal Model Validation. While it is desired to conduct temperature measurement during actual LAML processes to validate the present thermal model, the chips gener-

Table 1 Thermophysical properties for silicon nitride and Inconel 718

Material	α_l	ε_{IR}	ρ (kg/m^3)	k (W/m K)	c_p (J/kg K)
Si_3N_4	0.75 [24,25]	0.95 [24,25]	3220 [22]	Linear function of temperature [22]	Third order polynomial of temperature [22]
Inconel 718	0.35–0.5 (300–900°C)	0.2 [10]	7950	Linear function of temperature [10]	Linear function of temperature [10]

Table 2 Conditions used in the heating tests for thermal model validation

Test	Heating 1	Heating 2	Heating 3
P_{laser} (W)	550	830	940

ated from milling clouds the workpiece and hence prevent a direct temperature measurement using the infrared camera during LAML. Instead, heating tests without material removal were conducted on the silicon nitride and Inconel 718 workpieces to verify the thermal model in the present study.

It has been well characterized through many theoretical and experimental studies that laser power has the most significant impact on the workpiece temperature among all the operating parameters in LAM [5,14,18]. The present thermal model also shows that laser power is the dominant parameter determining the workpiece temperature during LAML. Therefore, laser power was selected as the primary variable in the heating tests. Other parameters were kept constant, including preheat time of $t_p=1.0$ s, laser beam size of 8×12 mm^2, and laser moving speed of $V=5$ mm/s.

During the heating tests with the conditions given in Table 2, the diode laser irradiates the workpiece surface normally and the infrared camera views the workpiece from an angle of about 45 deg. Three points, P1, P2 and P3, are defined along the path of the laser beam center for temperature history comparisons between the experimental measurements and thermal model predictions. The three points were located at 10 mm, 25 mm, and 35 mm, respectively, from the starting position of the laser beam center.

The thermal model was also validated by comparing thermal model results with measurements. Within prismatic workpieces, thermocouples were spot welded directly onto a sample of Inconel 718. The number of thermocouples and the thickness of the workpiece varied between experiments. The thermocouple locations on the 4.5 mm thick workpiece are shown in Fig. 4, with distances measured from the centerline of the laser track.

3.3 LAML Test Matrix for Si_3N_4. Compared to other operating parameters such as cutting speed and feed, workpiece temperature has been found having the most significant influence on the material behavior during LAM. The material removal temperature (T_{mr}), which is defined as the average workpiece temperature at the material removal zone as shown in Fig. 1, has been employed as a quantitative variable to evaluate the effect of workpiece temperature on LAM results [6,13,14].

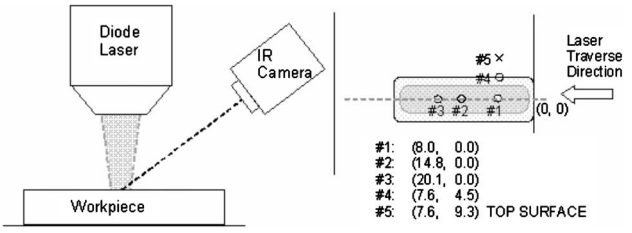

Fig. 4 Schematic of the laser heating setup (*a*) for prismatic model with (*b*) thermocouple locations on the workpiece with respect to laser heating track.

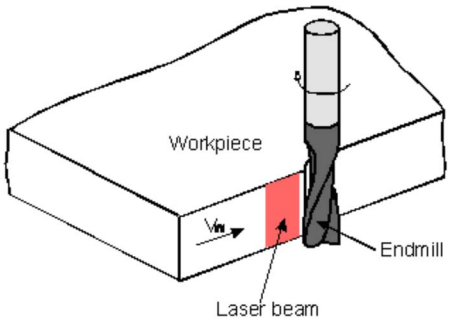

Fig. 5 Sketch of the experimental setups for the LAML of silicon nitride

The previous work also showed that the value of T_{mr} for LAM needs to be controlled within a window to obtain desired machining results. The present study used the thermal model to design experimental parameters, so that T_{mr} varies as the primary variable within a reasonable window, for instance, approximately 1100–1400°C for silicon nitride. Another important parameter in LAM is the lead distance between the laser beam and the cutting tool. As the lead distance increases, the delay between the laser heating and the material removal increases and causes a significant temperature drop on the surface. However, a proper delay is necessary to allow the heat to penetrate into the workpiece, so that the workpiece material within the depth of cut is heated to the desired temperature.

While the thermal model was developed for a general case of LAML as shown in Fig. 1, the actual LAML tests were carried out on the setup shown in Fig. 5, where the side cutting edge of the end mill was used to perform the material removal, because this setup can minimize the temperature gradient in the material removal zone and hence improve LAML results. The test matrix (Table 3) used laser power as the primary operating variable to achieve different material removal temperatures, while other operating parameters were kept constant through all the LAML experiments. The material removal temperatures shown in Table 3 were predicted using the present thermal model, since experimental determination of this value is difficult due to the rotation of the tool and the poor accessibility to the material removal zone.

The operating parameters for LAML consist of machining and laser parameters. The machining parameters are depth of cut, cutting length, spindle speed, and feed rate, which were fixed in the LAML experiments at $d=0.4$ mm, $L_c=20$ mm, $N=10\,000$ rpm, and $\dot{f}=3.3$ mm/s, respectively. Besides laser power P_{laser}, the laser parameters include laser-tool lead L_{lead}, preheat time t_p, and laser beam size S_b.

3.4 LAML Text Matrix for Inconel 718. For LAML of Inconel 718, a high spindle speed, low feed, and small depth of cut were used to maintain the cutting forces low. The experimental setup is shown in Fig. 3, in which a slot shown in Fig. 1 is created

Table 3 Operating parameters used in the LAML of silicon nitride

Test	P_{laser} (W)	T_{mr} (°C)	d (mm)	L_c (mm)	N (rpm)	$\dot{f}$ (mm/s)	t_p (s)	L_{lead} (mm)	S_b (mm)
LAML1	1000	1150	0.4	20	6	3.3	6	3.0	14×9
LAML2	1100	1210	0.4	20	6	3.3	6	3.0	14×9
LAML3	1200	1280	0.4	20	6	3.3	6	3.0	14×9
LAML4	1300	1360	0.4	20	6	3.3	6	3.0	14×9

Table 4 Experimental conditions for LAML of Inconel 718

Test No.	V (m/s)	f_r (mm/th)	d (mm)	N (rpm)	P_{laser} (W)	T_{mr} (°C)	Model: α_l
INM1	6.76	0.0125	0.22	10170	—	—	—
INM2	6.76	0.0125	0.28	10170	380	400	0.38
INM3	6.76	0.0125	0.25	10170	490	520	0.49
INM4	6.76	0.0125	0.38	10170	980	1200+	0.90

by the machining process. The experimental matrix shown in Table 4 was created to investigate the effects of changes in the material removal zone temperature. Multiple experiments were performed at each set of parameters with similar cutting forces and tool wear.

4 Experimental Results and Discussions

4.1 Temperature Measurements and Model Validation. Excellent agreements between the predicted and measured temperature histories for Heating1 are shown in Fig. 6, where Tmax_Meas and Tmax_Pred stand for the measured and the predicted maximum temperature under the laser beam, respectively, while Tp1, Tp2, and Tp3 are the temperatures at the fixed measurement locations specified in Sec. 3.2. A lower cutoff is observed in the measured temperatures, since the IR camera has the measurement range of 350–1500°C. During the 1 s preheating, a rapid rise of the maximum temperature T_{max} occurs under the stationary laser irradiation. After the preheating, the laser beam starts moving and the maximum temperature approaches a semi-constant value. Both the predictions and measurements show a slow and then sharp increase in Tp1 at the measuring Point P1 as the center of the laser beam moves to the point. After the laser beam passes over this point, its temperature drops gradually due to conduction within the workpiece as well as radiation and convection to surrounding. The temperature histories at P2 and P3, Tp2 and Tp3, follow a similar trend, which indicates that each point in the moving path of the laser beam center experiences similar temperature evolution.

Figure 7 displays the comparisons between the measured and predicted T_{max} histories for all the three heating tests. In general, the thermal model predictions match corresponding temperature measurements very well in each case. A similar result was also achieved for Inconel 718 as shown in Fig. 8, where the symbol of "Th" means thermocouple measurements at the locations sketched in Fig. 4. The nice comparisons between the two temperature fields also indicate that the present thermal model can accurately predict workpiece temperatures during LAML.

4.2 LAML of Silicon Nitride. Successful LAML of silicon nitride was achieved in each of the experiments listed in Table 3. Figure 9 shows an example of the silicon nitride parts produced under the conditions of LAML2. The section view of the silicon nitride workpiece shows the well defined geometry of the ceramic workpiece produced by the LAML process. Virtually, no crack was observed under the machined surface.

The TiAlN coated tools were examined with an optical microscope after each LAML test. The influence of laser power on the tool wear during LAML is illustrated in Fig. 10, which shows the

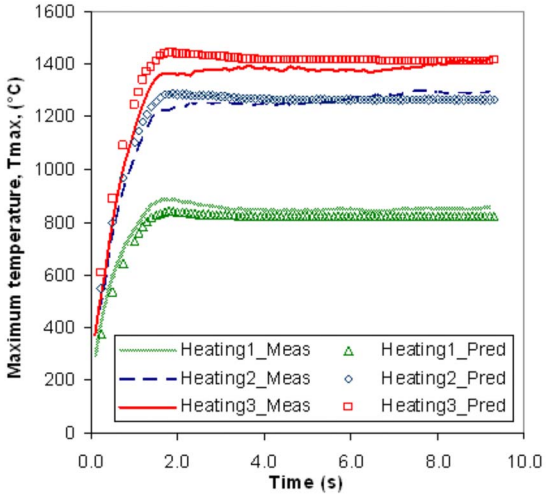

Fig. 7 Predicted T_{max} compared to IR camera measurements for Si_3N_4 workpiece

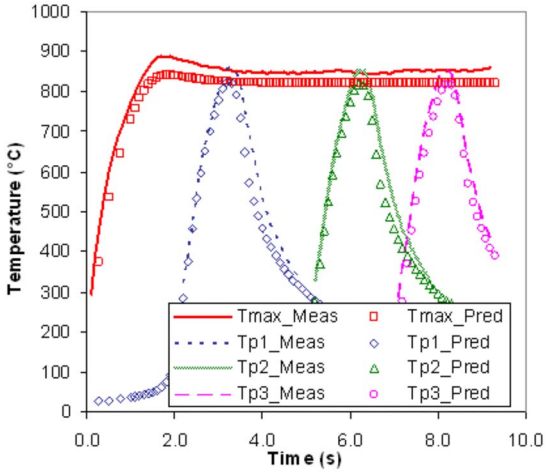

Fig. 6 Predicted temperatures compared to IR camera measurements for Heating1

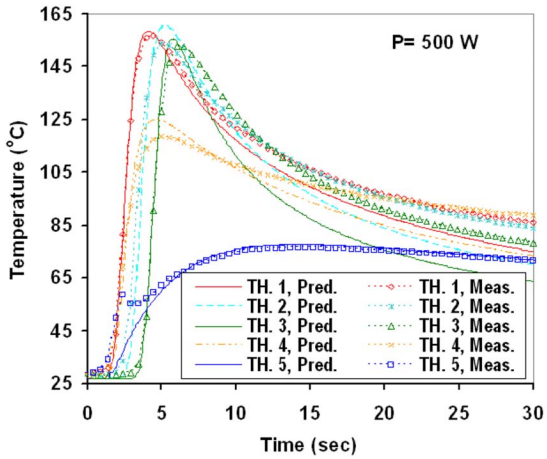

Fig. 8 Predicted temperatures compared to thermocouple measurements for Inconel 718 workpiece

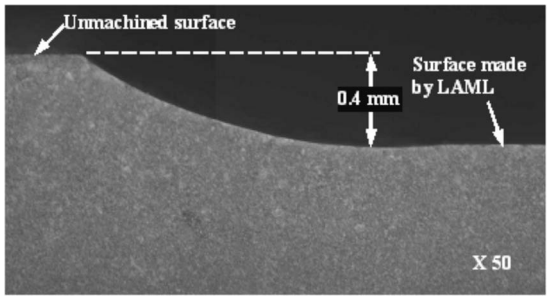

Fig. 9 Optical micrograph of a section view for a workpiece produced by LAML2

micrographs of the tools after 20 mm machining. The flank wear for the end mill was measured at the center of the side cutting edge for the experimental setup shown in Fig. 5. At the lowest laser power (1000 W), the tool wore out very fast due to the retained high strength of the workpiece material during LAML1, which suggests that the silicon nitride workpiece was not softened enough at the material removal temperature of about 1150°C. With the increase in laser power and hence material removal temperature, the tool wear significantly reduced and the wear pattern changed to more uniform abrasive wear at the conditions of LAML2 and LAML3. However, further increasing laser power to 1300 W (LAML4) caused more wear with chipping on the tool, because the tool was weakened due to over heating. The tool wear shown in Fig. 11 indicates that the proper range of material removal temperature, from about 1200°C to 1300°C, is rather narrow in LAML of silicon nitride using TiAlN coated carbide tools, while good tool life was found in a much wider range for LAM of silicon nitride using polycrystalline cubic boron nitride (PCBN)

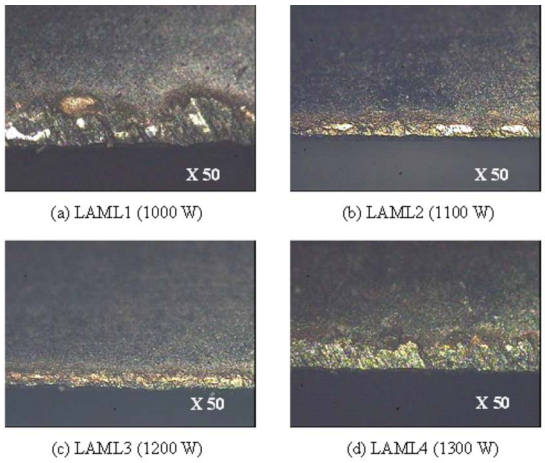

Fig. 10 Flank wear of the TiAlN coated carbide tools after 20 mm cutting of LAML

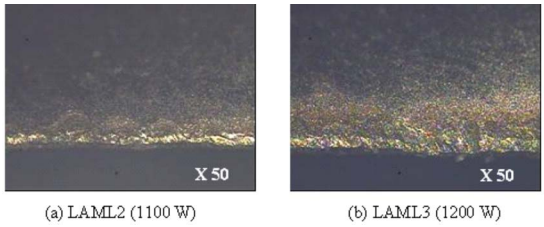

Fig. 11 Flank wear of the TiAlN coated carbide tools after 60 mm cutting of LAML

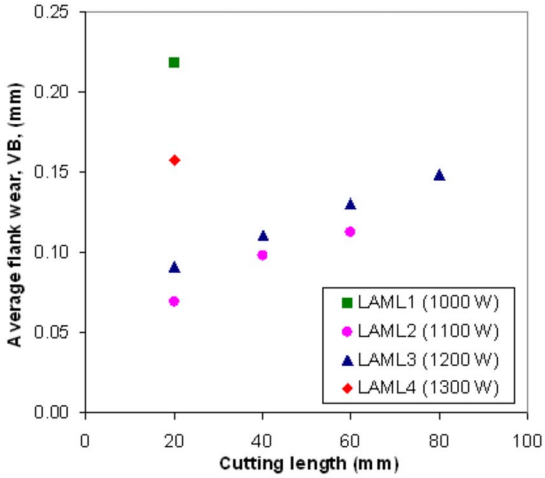

Fig. 12 Flank wear of the TiAlN coated carbide tools during LAML of silicon nitride

tipped tools.

For LAML2 and LAML3, several experiments were conducted to continue the tool wear test and verify the repeatability of the experiments. Slow increases in flank wear (Fig. 12) and no change on the tool wear pattern (Fig. 11) were observed under the conditions of the two cases. The steady development of tool wear indicates that the tool life may be obtained by extrapolating the trend of tool wear shown in Fig. 12. For a typical tool wear limit of VB=0.3 mm, the tool life is projected to be about 260 and 240 mm cutting for LAML2 and LAML3, respectively.

As shown in Fig. 13, good surface finish, R_a=0.55–0.80 μm, was obtained on the silicon nitride workpiece produced by the LAML experiments. The slow increases in surface roughness with cutting length for LAML2 and LAML3 were caused by the gradual development of tool wear. Larger surface roughness found in LAML1 may be explained by the excessive tool wear and low material removal temperature in this case.

4.3 LAML of Inconel 718

4.3.1 Cutting Forces. Forces were sampled at a frequency of 10 kHz, which allows 60 readings/rev. The maximum force during every revolution was averaged, and is plotted against the laser power in Fig. 14. The *Z*-direction coincides with the depth of the

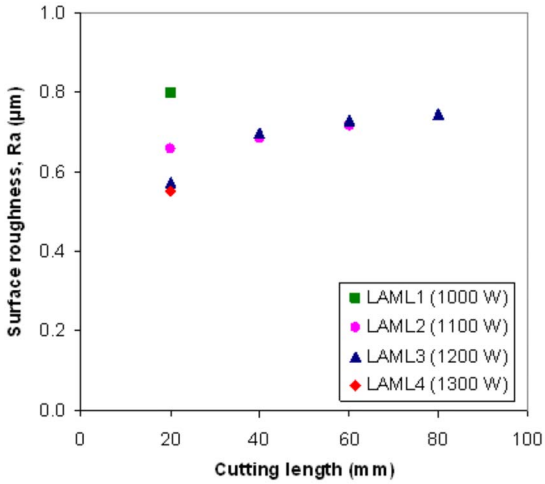

Fig. 13 Average surface roughness of the silicon nitride workpiece made by LAML

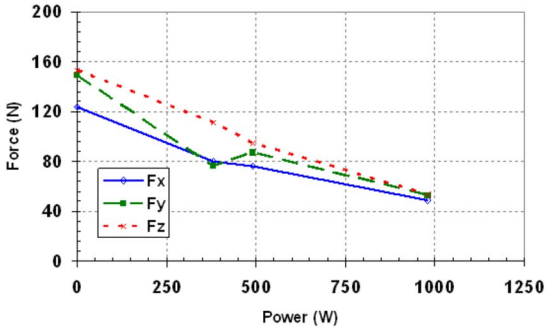

Fig. 14 Average maximum measured forces along the *X*, *Y*, and *Z* directions

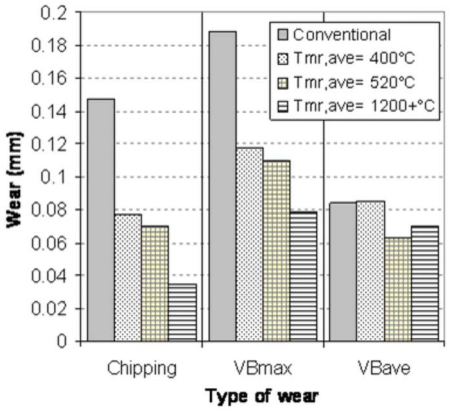

Fig. 16 Tool wear on the SiC reinforced alumina insert after machining 20 mm Inconel 718

groove (spindle axis), and the *Y*-direction coincides with the direction of travel, while the *X*-direction is perpendicular to the length of the cut groove. The forces decrease as the temperature increases, with the largest decrease seen between conventional machining and LAM, $P=380$ W, INM2.

Figure 15 shows the comparison of the cutting forces as a function of time for both LAM, $T_{mr}=400°C$ and conventional milling. The cutting forces during conventional milling increase very rapidly due to the higher material strength and also the increased ability of the workpiece to strain harden. During LAM, even at "low temperatures," the increase in cutting forces is very gradual.

4.3.2 Tool Wear. The tool wear is mostly confined to the negative hone on the nose of the tool until significant chipping occurs, which will ultimately be the mode of failure. Figure 16 shows the comparison of the tool wear for the various machining conditions. The average flank wear is very similar for all the temperatures tested, including conventional machining, but chipping decreases significantly from conventional to LAM, $T_{mr}=400°C$ and then decreases significantly again at high powers, INM4. The decrease in chipping from the laser assist allows a small tool radius to be used for milling of high temperature alloys, where typically only round ceramic tools possessing enough strength are used to efficiently mill these materials.

It was observed that during INM2 and INM3, only a 5 mm wide area in the center of the groove ahead of the cutting tool showed visible effects of heating, while in INM4 almost the entire groove width showed visible effects of heating. Perhaps, an alternate placement of the laser beam—favoring the tool entrance side, or perhaps the tool exit—would decrease the chipping at lower powers. Also, a sufficient preheating cycle is essential to reduce the amount of chipping on the tool. If the preheat was not long enough, or positioned too far from the edge of the workpiece during LAM, the amount of chipping was comparable to that of conventional machining. Pictures of the tools are shown in Fig. 17 for a short machining distance. It can easily be observed that the chipping in the tool decreases as T_{mr} is increased.

It appears that INM4 would be the ideal condition for machining due to both the low cutting forces and low tool wear, but this high power melted the surface of the workpiece and caused a heat affected zone more than 3 mm deep in the workpiece.

The surface roughness generally improves with an increase in T_{mr} as shown in Fig. 18, where the average surface roughness decreases from 0.35 μm for conventional milling to 0.18 μm at $T_{mr}=520°C$. At higher temperatures, such as INM4, the surface oxidizes, degrading the surface quality and increasing the surface roughness, as was also shown by Leshock et al. [26], occurring at temperatures above 530°C.

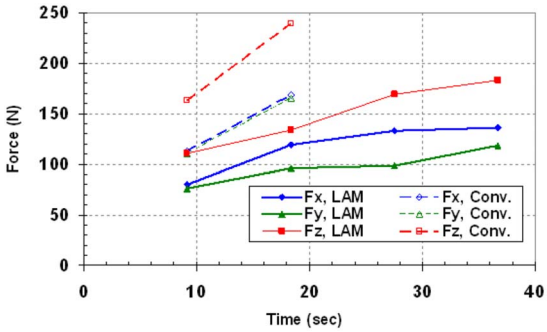

Fig. 15 Measured cutting forces as a function of machining time at $V=6.76$ m/s, $f_r=0.0125$ mm/rev, $T_{mr}=400°C$ (INM1, INM2)

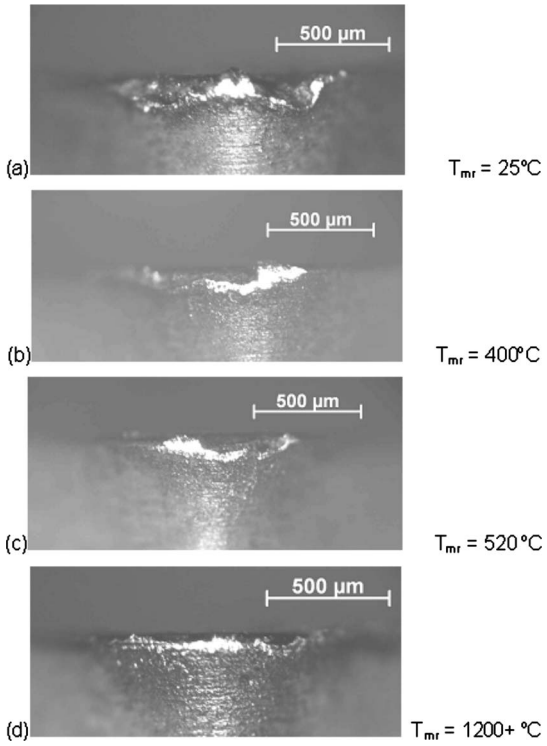

Fig. 17 Nose of the SiC reinforced alumina insert after 9 s of machining time for Inconel 718 (*a*) conventional machining and various T_{mr} experiments: (*b*) $T_{mr}=400°C$, (*c*) $T_{mr}=520°C$, and (d) $T_{mr}=1200°C$

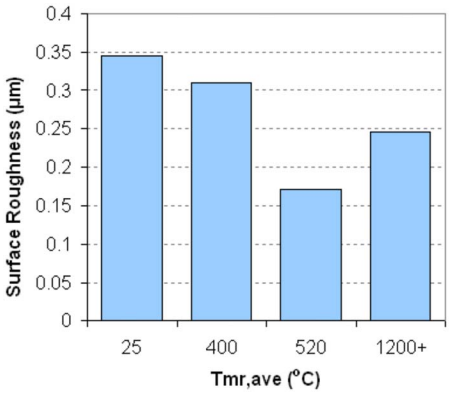

Fig. 18 Average surface roughness as a function of laser power during milling of Inconel 718

5 Conclusions

A transient, three-dimensional thermal model for LAML has been developed and validated through surface temperature measurements using an infrared camera and embedded thermocouples. The thermal model can provide the transient temperature distributions within the workpiece with changing geometry during LAML. LAML of silicon nitride was successfully conducted using TiAlN coated carbide tools by elevating the material removal zone temperature to 1200–1300°C. The good results in the LAML experiments, in terms of good surface finish, repeatable performance, and acceptable tool wear, have shown the feasibility of LAML of silicon nitride. LAML of Inconel 718 also yielded a substantial improvement of machinability. LAM with the material temperature elevated to 520°C resulted in 40–50% reduction in cutting force, over 50% reduction in tool chipping, and twofold improvement in surface roughness.

Acknowledgment

The authors wish to gratefully acknowledge the financial support provided by the National Science Foundation (Grant No.IIP0538786) and the State of Indiana 21st Century R&T Fund.

Nomenclature

c_p = specific heat, J/kg K
d = depth of cut, mm
$\dot{f}$ = feed rate, mm/s
h = enthalpy, J/kg
k = thermal conductivity, W/m K
L_c = cutting length, mm
L_{lead} = laser-tool lead, mm
N = spindle speed, rpm
P_{laser} = laser power, W
q''_{conv}, q''_{rad} = convection, radiation heat flux, W/m^2
q''_l, q''_m = heat flux from laser irradiation, machining heat generation, W/m^2
x, y, z = Cartesian coordinate directions
R_a = average surface roughness, μm
S_b = diode laser beam size (x,y), mm
t = time, s
t_p = preheat time, s
T = temperature, °C
T_{ini} = workpiece initial temperature, °C
T_{mr} = average material removal temperature, °C
T_{max} = maximum temperature, °C
V = laser feed rate, mm/s
VB = average flank wear, mm

Greek Symbols

α_l = absorptivity of the workpiece surface to the laser irradiation
ε = total emissivity
ε_{IR} = spectral emissivity at the IR camera measurement wavelength (8–9 μm)
ρ = density, kg/m^3

References

[1] König, W., and Zaboklicki, A. K., 1993, "Laser-Assisted Hot Machining of Ceramics and Composite Materials," *International Conference on Machining of Advanced Materials*, Gaithersburg, MD, NIST Special Publication, Vol. 847, pp. 455–463.
[2] König, W., and Wagemann, A., 1993, "Machining of Ceramic Components: Process-Technological Potentials," *Machining of Advanced Materials*, NIST Special Publication, Vol. 847, pp. 3–16.
[3] Rozzi, J. C., Krane, M. J. M., Incropera, F. P., and Shin, Y. C., 1995, "Numerical Prediction of Three-Dimensional Unsteady Temperatures in a Rotating Cylindrical Workpiece Subjected to Localized Heating by a Translating Laser Source," *1995 ASME International Mechanical Engineering Conference and Exposition*, San Francisco, CA, HTD Vol. 317-2, pp. 399–411.
[4] Shin, Y. C., Lei., S., Pfefferkorn, F. E., Rebro, P., and Rozzi, J. C., 2000, "Laser-Assisted Machining: Its Potential and Future," Mach. Technol., **11**(3), pp. 1–6.
[5] Rozzi, J. C., Pfefferkorn, F. E., Shin, Y. C., and Incropera, F. P., 2000, "Experimental Evaluation of the Laser Assisted Machining of Silicon Nitride Ceramics," ASME J. Manuf. Sci. Eng., **122**(4), pp. 666–670.
[6] Lei, S., Shin, Y. C., and Incropera, F., 2001, "Experimental Investigation of Thermo-Mechanical Characteristics in Laser-Assisted Machining of Silicon Nitride Ceramics," ASME J. Manuf. Sci. Eng., **123**, pp. 639–616.
[7] Jau, B. M., Copley, S. M., and Bass, M., 1980, "Laser Assisted Machining," SME Technical Paper MR80-846.
[8] Rajagopal, S., Plankenhorn, D. J., and Hill, V. L., 1982, "Machining Aerospace Alloys With the Aid of a 15 kw Laser," Journal of Applied Metalworking, **2**(3), pp. 170–184.
[9] Bass, M., Beck, D., and Copley, S. M., 1978, "Laser Assisted Machining," *Fourth European Electro-Optics Conference*, Utrecht, Netherlands, pp. 233–240.
[10] Anderson, M., Patwa, R., and Shin, Y. C., 2006, "Laser-Assisted Machining of Inconel 718 With an Economic Analysis," Int. J. Mach. Tools Manuf., **46**, pp. 1879–1891.
[11] Anderson, M., and Shin, Y. C., 2006, "Laser-Assisted Machining of P550 With an Economic Analysis," Proc. Inst. Mech. Eng., Part B, **220**(12), pp. 2055–2067.
[12] Klocke, F., and Bergs, T., 1997, "Laser-Assisted Turning of Advanced Ceramics," Proc. SPIE, **3102**, pp. 120–130.
[13] Rebro, P., Shin, Y. C., and Incropera, F. P., 2002, "Laser Assisted Machining of Reaction Sintered Mullite Ceramics," ASME J. Manuf. Sci. Eng., **124**, pp. 875–885.
[14] Pfefferkorn, F. E., Shin, Y. C., Tian, Y., and Incropera, F. P., 2004, "Laser-Assisted Machining of Magnesia-Partially Stabilized Zirconia," ASME J. Manuf. Sci. Eng., **126**, pp. 42–51.
[15] Rozzi, J. C., Pfefferkorn, F. E., Incropera, F. P., and Shin, Y. C., 2000, "Transient, Three-Dimensional Heat Transfer Model for the Laser Assisted Machining of Silicon Nitride: I-Comparison of Predictions With Measured Surface Temperature Histories," Int. J. Heat Mass Transfer, **43**, pp.1409–1424.
[16] Rozzi, J. C., Incropera, F. P., and Shin, Y. C., 2000, "Transient, Three-Dimensional Heat Transfer Model for the Laser Assisted Machining of Silicon Nitride: II-Assessment of Parametric Effects," Int. J. Heat Mass Transfer, **43**, pp. 1425–1437.
[17] Pfefferkorn, F. E., Incropera, F. P., and Shin, Y. C., 2005, "Heat Transfer Model of Semi-Transparent Ceramics Undergoing Laser-Assisted Machining," Int. J. Heat Mass Transfer, **48**(10), pp. 1999–2012.
[18] Tian, Y., and Shin, Y. C., 2006, "Thermal Modeling for Laser-Assisted Machining of Silicon Nitride Ceramics with Complex Features," ASME J. Manuf. Sci. Eng., **128**, pp. 425–434.
[19] Skvarenina, S., and Shin, Y. C., 2006, "Laser-Assisted Machining of Compacted Graphite Iron With Microstructural Analysis," Int. J. Mach. Tools Manuf., **46**, pp. 7–17.
[20] Jeon, Y., and Pfefferkorn, F. E., 2008, "Effect of Laser Preheating the Workpiece on Micro-End Milling of Metals," ASME J. Manuf. Sci. Eng., **130**, pp. 011004.

[21] Shen, X., Liu, W. J., and Lei, S., 2005, "Three-Dimensional Thermal Analysis for Laser Assisted Milling of Silicon Nitride Ceramics Using FEA," *Proceedings of 2005 ASME International Mechanical Engineering Congress and Exposition*, Nov. 5–11, Orlando, FL, Vol. 16(1), pp. 445–452.
[22] Taylor, R. E., Groot, H., and Ferrier, J., 1998, "Thermophysical Properties of Si_3N_4," TPRL Report No. 2128.
[23] Patankar, S. V., 1980, *Numerical Heat Transfer and Fluid Flow*, Hemisphere, New York.
[24] 1972, *Thermophysical Properties of Matter*, Y. S. Touloukian and D. P. DeWitt eds., IFI/Plenum, New York, Vol. 8.
[25] 1988, *Theory and Practice of Radiation Thermometry*, D. P. Dewitt, and G. D. Nutter, eds., Wiley, New York, pp. 174.
[26] Leshock, C. E., Kim, J. N., and Shin, Y. C., 2001, "Plasma Enhanced Machining of Inconel 718: Modeling of Workpiece Temperature With Plasma Heating and Experimental Results," Int. J. Mach. Tools Manuf., **41**, pp. 877–897.